Advances in
Geo-Energy Research

Vol. 17, No. 1, p. 68-81, 2025

Original article

Impacts of multi-scale water-rock interaction on mineral alteration, mechanical weakening and pore-fracture evolution in marine shales

Ying Mu[1,2], Caineng Zou[3]*, Zhiming Hu[3], Xianggang Duan[3], Qiulei Guo[4], Zhenhua Jing[3]*

[1] *State Key Laboratory of Coal Mine Disaster Dynamics and Control, Chongqing University, Chongqing 400044, P. R. China*

[2] *Advanced Energy Storage Technology Research Center, Shenzhen Institute of Advanced Technology, Chinese Academy of Sciences, Shenzhen 518055, P. R. China*

[3] *Research Institute of Petroleum Exploration and Development, PetroChina, Beijing 100083, P. R. China*

[4] *School of Earth Resources, China University of Geosciences, Wuhan 430074, P. R. China*

Keywords:
Water-rock interaction
secondary structures
mineral alteration
mechanical weakening
pore-fracture evolution

Cited as:
Mu, Y., Zou, C., Hu, Z., Duan, X., Guo, Q., Jing, Z. Impacts of multi-scale water-rock interaction on mineral alteration, mechanical weakening and pore-fracture evolution in marine shales. Advances in Geo-Energy Research, 2025, 17(1): 68-81.
https://doi.org/10.46690/ager.2025.07.06

Abstract:
Water-rock interaction triggered by drilling and fracturing fluid retention in shale gas reservoirs induces secondary processes and the subsequent alteration of rock physical properties, critically modulating reservoir productivity. In this study, X-ray diffraction, nanoindentation, focused ion beam-scanning electron microscopy, and micro-computed tomography were utilized to characterize and analyze the mineral alteration, mechanical weakening and pore-fracture evolution of marine shale in the Longmaxi Formation, Sichuan Basin. The results reveal that the water-rock interaction preferentially dissolves clay minerals (mainly illite), feldspars and pyrite via hydration and redox reactions while promoting quartz and carbonate mineral recrystallization. The hydration-dissolution-precipitation process significantly weakens the rock mass by reducing cohesion and the friction angle. This mechanical degradation is evidenced by a substantial decrease in elastic modulus, exhibiting pronounced anisotropy relative to stratifications. The resultant heterogeneous stress fields initiate and propagate secondary pores and fractures, dramatically increasing the number, volume and surface area of pores. These newly formed structures integrate with pre-existing pore-fracture networks, markedly elevating overall porosity and enhancing interconnectivity, which consequently amplifies permeability by orders of magnitude. Additionally, water preferentially enters the reservoir through stratification, and the associated difference in water-rock interaction strength further enhances the heterogeneity of structural and mechanical heterogeneity. These findings link micro-scale physical-chemical reactions with the meso-scale mechanical properties and macro-scale pore-fracture structures, emphasize the key role of water-rock interaction in reshaping reservoir characteristics, and provide important insights for optimizing hydraulic fracturing strategies and improving shale gas recovery.

1. Introduction

In the shale gas production industry, horizontal drilling and hydraulic fracturing are the most popular methods to promote the migration of shale gas from the reservoir to the wellbores (Zhou et al., 2016b; Song et al., 2022). As part of these industrial processes, multiple fluids, such as drilling fluid, completion fluid, cementing fluid, and fracturing fluid

---

*Corresponding author.

E-mail address: muying1994@163.com (Y. Mu); zcn@petrochina.com.cn (C. Zou); huzhiming69@petrochina.com.cn (Z. Hu); duanxg69@petrochina.com.cn (X. Duan); guoqiulei@cug.edu.cn (Q. Guo); zhenhua.jing@uqconnect.edu.au (Z. Jing).

Yandy Scientific Press

2207-9963

Received May 21, 2025; revised June 16, 2025; accepted July 2, 2025; available online July 6, 2025.

are injected into the reservoir, which can inevitably enter the shale matrix under the actions of positive pressure difference, chemical potential difference, and capillary force (Yang et al., 2023). The intimate contact of water and shale can in turn trigger comprehensive physical and chemical processes, referred as Water-Rock Interaction (WRI), which could bring profound alteration to the shale reservoir properties (Ma et al., 2016; Sui et al., 2018; Hua et al., 2021; Lin et al., 2022). It has been confirmed that WRI can lead to the decomposition, hydration and expansion of some minerals (clay minerals in particular), the oxidation of pyrite, and changes in the energy and pressure on rock surface (Røyne et al., 2015; Chen et al., 2017; Feng et al., 2020; Lu et al., 2020). As a result, the mechanical properties of shale, such as compressive strength, brittleness index and elastic modulus, are further weakened, which affects the expansion of pore-fracture network (Dautriat et al., 2016; Kang et al., 2016; Zhong et al., 2019; Velcin et al., 2020). These changes deeply transform the native occurrence modalities and migration dynamics of methane within the reservoir (Song et al., 2022; Zou et al., 2024). Thus, systematically investigating the WRI-induced transformations, particularly in a quantitative manner, is critical for optimizing shale gas recovery and enhancing reservoir reconstruction.

Existing studies have widely demonstrated that WRI in shale can be affected by minerals, fracturing fluid composition and action time (Roshan et al., 2015; Cai et al., 2024). Clay minerals (especially montmorillonite and its mixed layer) have strong imbibition ability, and some metal cations in formation water readily accumulate on the surface of mineral particles (Liu et al., 2016b). The cation charge is dissolved and exchanged, changing the attraction and repulsion between the mineral particles, as well as weakening the cohesion, internal friction angle, compressive strength and structural integrity of the rock (Tang et al., 2024). Therefore, shales with high clay mineral content have been proposed to be more susceptible to WRI (Zhong et al., 2019). Some aluminosilicate and carbonate minerals can also be dissolved in water and recrystallized at other locations. The shedding of minerals caused by clay expansion and mineral dissolution can produce new pores and fractures (Wang et al., 2020). In the oxygen-rich environment, the chemical oxidation of organic matter may form new pores (Jing et al., 2018a, 2018b). These secondary reconstructions further expand the seepage channels of the reservoir, thereby improving the gas flow capacity (Xu et al., 2023). In addition, due to the complex stratifications, shale has obvious permeability anisotropy and water is more likely to enter the matrix along the stratifications, which may cause differences in the strength of WRI (Heng et al., 2020).

Experimental techniques like spontaneous imbibition tests and mercury intrusion porosimetry have elucidated the fluid distribution patterns and pore-fracture characteristics (Kang et al., 2016). However, these studies have failed to systematically quantify the differences in reaction mechanisms and reaction strengths among different minerals with water (Kelly et al., 2016). Previous studies have documented the macroscopic effects of WRI, such as reductions in compressive strength and brittleness index (Lyu et al., 2018; Zhong et al., 2019). In fact, the microscopic mechanical properties can more accurately couple mineral hydration mechanisms with the generation of pore-fracture networks (Wang et al., 2020; Li et al., 2022). Besides, traditional analytical methods are often unable to capture the anisotropic nature of microscopic mechanical and hydraulic responses, particularly under stratified conditions (Zhou et al., 2016a; Heng et al., 2020). These gaps hinder gaining a holistic understanding of multi-scale impacts on reservoir reconstruction. Therefore, it is necessary to systematically reveal the microscopic reaction mechanism of different minerals and water in marine shale, clarify their comprehensive effects on the microscopic mechanical properties and microscopic pore structure of rocks, and subsequently analyze these effects on the macroscopic pore-fracture network.

In this study, X-Ray Diffraction (XRD), nanoindentation, Focused Ion Beam Scanning Electron Microscopy (FIB-SEM), and Micro-Computed Tomography (μCT) are used to conduct a comprehensive analysis of WRI on marine shale from the Longmaxi Formation, Sichuan Basin. The differences in mineral hydration strength are quantified, and the correlation between mechanical weakening and pore-fracture network expansion is analyzed. In addition, the relationship between micro-scale hydration mechanism and macro-scale porosity and permeability enhancement is established, and the anisotropy of WRI is clarified. The findings provide a robust theoretical foundation for informing and optimizing the development strategies of shale gas wells, and help to enhance their operational efficiency and economic viability.

2. Samples and methods

2.1 Samples

The Lower Cambrian Qiongzhusi Formation, Upper Ordovician Wufeng Formation, and Lower Silurian Longmaxi Formation are deposited within the Sichuan Basin, which constitutes a pivotal exploration region for marine shale gas in southern China (Jin et al., 2018). For the purpose of this study, a full-diameter marine shale core retrieved from the Longmaxi Formation within the Changning Block of the Sichuan Basin was chosen. The sample was obtained at an approximate burial depth of 2,332.16 m. Subsequently, crushed rock samples, thin-section rock samples, and one-inch standard cores were prepared from the full-diameter core, and a comprehensive suite of experimental analyses, including XRD, nanoindentation, FIB-SEM, and μCT, was systematically conducted to characterize the mineralogical composition, mechanical properties, and pore-fracture network of samples (Fig. 1).

2.2 Methods

2.2.1 X-ray diffraction

XRD can determine not only the chemical composition of a sample material but also its crystal structure, crystal defects, and crystal parameters (Yang et al., 2020; Das et al., 2021). XRD can be regarded as the reflection of incident X-rays by parallel and adjacent atoms inside the crystal (Liu et al., 2023). According to the Bragg equation $n\lambda = 2d\sin\theta$, the relationship between X-ray parameters and cell parameters

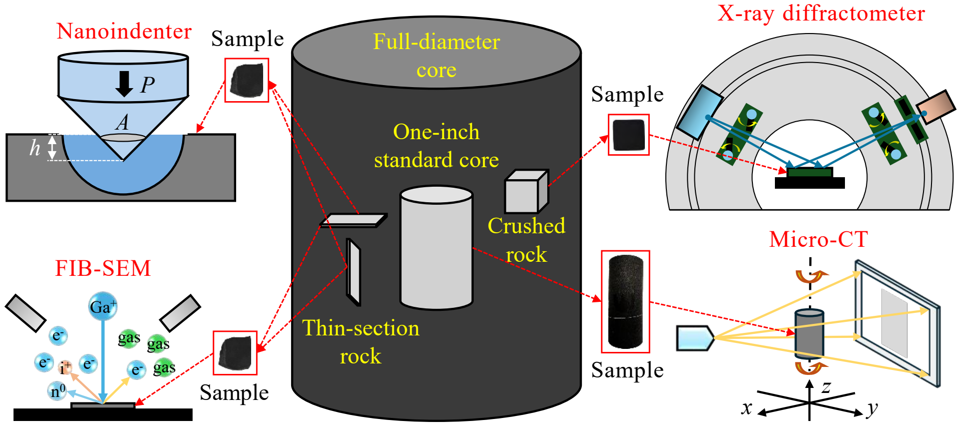

Fig. 1. Experimental samples and methods.

can be determined (Elton and Jackson, 1966). The X-ray with a fixed wavelength of λ is used to impact the sample crystal, and the interplanar spacing d can be obtained according to the reflection order n and the grazing angle θ of the diffracted X-ray (Molčanov and Stilinović, 2014). Next, the relative content of different minerals can be established according to the intensity information of diffraction X-ray.

Selected rock samples were crushed into small particles and ground to a mesh size below 200 for use as XRD experimental samples. The samples were divided into two equal parts: The first part was directly analyzed, while the second part was soaked in distilled water (to prevent interference from other ions) for 96 h before analysis. For whole rock samples, the pretreatment process involved identification, solvent extraction to remove oil, crushing, preparation, and slicing. Meanwhile, for clay samples, the pretreatment process included identification, solvent extraction to remove oil, crushing, soaking, siphoning, centrifugal precipitation, and tableting.

The mineral composition of shale was analyzed by the RINT-TTR3 diffractometer of Rigaku. Cu target (monochrome) was used, the rotation angle was $2.5^\circ \sim 60^\circ$, the tube voltage was 40 kV, and the tube current was 100 mA. Quantitative analysis was carried out by step scanning. The scanning speed was set to 0.25°/min, and sampling interval was set to 0.01°. Given the robustness and exceptional hydration resistance exhibited by quartz, coupled with the requirement for aluminosilicates to undergo a high-temperature process to attain a stable quartz structure, it is reasonable to postulate that the absolute mass of quartz remains constant throughout the WRI process. By leveraging this invariance in quartz mass as a baseline, we can precisely quantify the alterations in the mass of other constituent minerals within a unit mass of shale.

2.2.2 Nanoindentation

Nanoindentation technology was first applied to homogeneous materials such as metals, glass and crystals, and then gradually used to measure the mechanical parameters of heterogeneous materials. It can measure the key mechanical parameters of materials at the microscopic scale (Liu et al., 2016a). The principle of nanoindentation is to apply a load of $0.1 \sim 500.0$ mN to the surface of the material by a diamond indenter and then use the load and displacement data to obtain the load-displacement curve ($P-h$ curve). The $P-h$ curve forms the basis for analyzing the microscopic deformation of materials and calculating the mechanical parameters of materials. By meticulously documenting the loading depth and force exerted by the probe throughout the loading-holding-unloading sequence conducted by the nanoindenter, it is feasible to derive the microscopic mechanical parameters of the indented location.

The hardness and equivalent elastic modulus of the material can be analyzed and calculated by using the $P-h$ curve as follows (Richter et al., 2000):

$$H=\frac{P_{\max}}{A} \tag{1}$$

$$E_r=\frac{S\sqrt{\pi}}{2\beta\sqrt{A}} \tag{2}$$

where H denotes the hardness, GPa; $P_{\max}$ denotes the maximum load value, mN; A denotes the contact area at the maximum load, nm^2; E_r denotes the equivalent elastic modulus, GPa; S denotes the contact stiffness, mN/nm; β denotes the indenter correction coefficient, dimensionless. For the commonly used Berkovich indenter, $\beta = 1.034$.

For nanoindentation investigations, ultra-flat shale sheets were prepared. Directions both vertical and parallel to the stratification were selected. Those samples were initially sliced into thin sections with a thickness about 10 mm. The surfaces of samples were progressively polished using silicon carbide sandpapers of 400, 600 and 1,500 mesh grades to achieve a high degree of smoothness. This was followed by a series of polishing steps using oil-based diamond suspensions of decreasing particle sizes (6, 3 and 1 μm), culminating in a final refinement by a precision argon ion beam polishing instrument to ensure optimal surface quality. The samples were then dried at 105 °C for 48 h and their mechanical properties were measured. Subsequently, the samples were immersed in simulated formation water (a calcium chloride solution with a concentration of 50,000 mg/L) for 96 h to promote water uptake and mitigate rock fragmentation. After

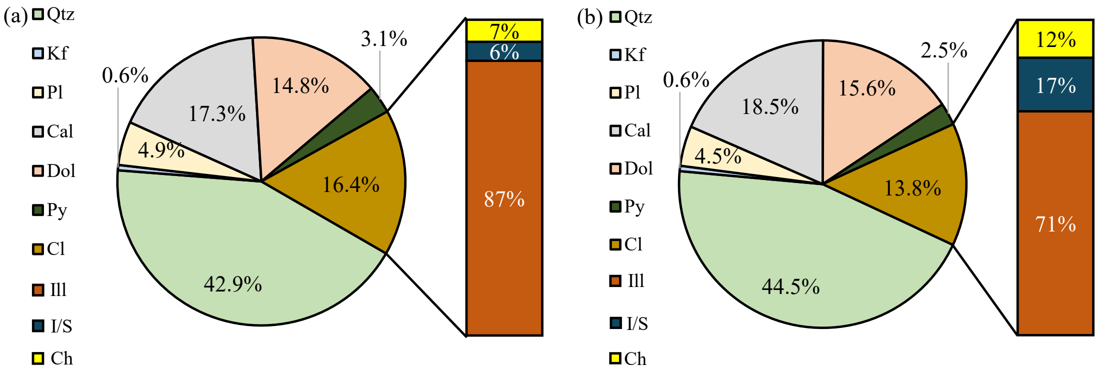

Fig. 2. Relative content of minerals (a) before and (b) after WRI. Qtz: Quartz; Kf: K-Feldspar; Pl: Plagioclase; Cal: Calcite; Dol: Dolomite; Py: Pyrite; Cl: Clay; Ill: Illite; I/S: Illite-smectite mixed layer; Ch: Chlorite.

this treatment, the mechanical properties of the saturated samples were evaluated.

The microscopic mechanical parameters of shale were measured by a Bruker Hysitron TI Premier nano-indentation instrument. For every sample, five 60×60 μm matrices were chosen and each matrix evenly suppressed 9 points. The maximum loading force was 10,000 μN, the loading and unloading time were 30 s, and the holding time was 5 s. $P-h$ curves for every point were acquired and the mechanical properties of each point were computed. In both the dry and wet states, the mechanical characteristics of shale samples were recorded in the directions parallel and vertical to stratifications. At the nanometer scale, mechanical parameters acquired via indentation points on the surface of diverse minerals exhibit inherent volatility. To mitigate measurement uncertainties, extensive replication of shale sample assessments is imperative. Therefore, this research adopted a rigorous mean statistical approach to analyze the collected data.

2.2.3 Focused ion beam scanning electron microscopy

FIB-SEM is a system that combines Focused Ion Beam (FIB) and Scanning Electron Microscope (SEM) functions (Kelly et al., 2016; Song et al., 2022). In this system, the electron beam is perpendicular to the sample stage and the ion beam has a certain angle with the sample stage. During the working process, the sample stage needs to be rotated to a position of 52°. The ion beam and the sample stage are in a vertical state, which is convenient for processing. The electron beam and the sample stage are at a certain angle, and the structure inside the cross-section can be observed.

The experimental samples of FIB-SEM were the same as for nanoindentation. This study mainly compared the differences in the microscopic pore structure of shale in the planes parallel and vertical to stratifications before and after the water-rock interaction. The surface morphology was examined using the Helios Nanolab 650 of FEI company, and the system had an imaging voltage of 5 kV and a maximum resolution of 0.8 nm.

2.2.4 Micro-computed tomography

CT uses cone-shaped X-rays to penetrate objects, enlarge images through objective lenses of different multiples and reconstruct a three-dimensional stereo model from X-ray attenuation images obtained by 360° rotation (Thibault and Elser, 2010). A CT image reflects the information of energy attenuation of X-ray in the process of penetrating the object, so it can truly reflect the pore structure and relative density inside the core (Garum et al., 2020). During scanning, the turntable drives the sample to rotate, and with each rotation having a certain angle, X-ray irradiation of the sample is performed to obtain a projection. A series of projection images obtained after rotating 360° were reconstructed to obtain a three-dimensional image of the core sample.

The μCT experimental sample is a cylindrical shale core with a diameter of one inch. Prior to WRI, the sample was dried at 105 °C for 96 h and then scanned to obtain initial three-dimensional structural information. Subsequently, the sample was placed in a core holder under a confining pressure of 45 MPa to simulate formation pressure. High-pressure water invasion was performed from one end of the core using simulated formation water (a calcium chloride solution with a concentration of 50,000 mg/L) at a pressure of 40 MPa to simulate hydraulic fracturing. The sample was then continuously soaked under pressure to replicate the process of working fluid invading the shale matrix. After the WRI, the sample was scanned again to obtain the final three-dimensional structural data.

The characteristics of shale pores and fractures were analyzed by a Zeiss MicroXCT-400 three-dimensional X-ray microscope. The maximum voltage of the ray tube of the μCT system was 300 kV, and the focal size was 2 μm. The utilization of Volume Graphics software facilitates a meticulous analysis of the grayscale variations within the three-dimensional data volume, enabling the extraction of crucial pore and fracture characteristics from shale sample.

3. Results

3.1 Minerals

Quartz (Qtz) was the predominant mineral in the raw samples (averagely c.a. 42.9%), followed closely by calcite (Cal, ∼17.3%), clay (Cl, ∼16.4%) and dolomite (Dol, ∼14.8%), with minor contributions from plagioclase (Pl, ∼4.9%), pyrite (Py, ∼3.1%) and K-feldspar (Kf, ∼0.6%) (Fig. 2(a)). After

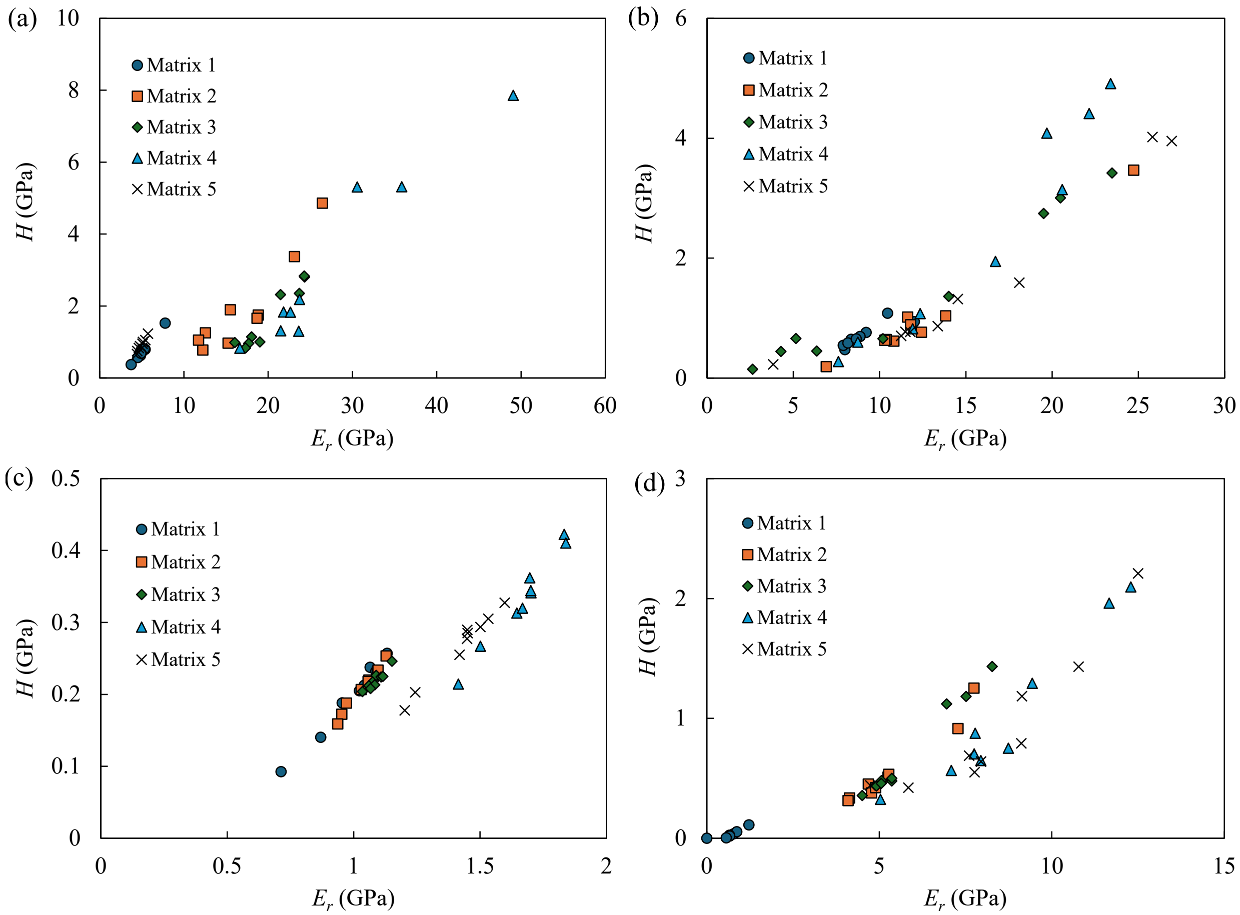

Fig. 3. Distribution of elastic modulus and hardness in directions (a) parallel and (b) vertical to stratification before WRI; distribution of elastic modulus and hardness in directions (c) parallel and (d) vertical to stratification after WRI.

WRI, the mass ratio of quartz increased to ∼44.5%, and that of calcite and dolomite also increased to ∼18.5% and ∼15.6%, respectively, while the relative contents of clay and pyrite decreased to 13.8% and 2.5%, respectively (Fig. 2(b)). Within the clay fraction, illite (Ill) dominated, averaging approximately 87%, with the proportions of illite-smectite mixed layer (I/S) and chlorite (Ch) being essentially equivalent (Fig. 2(a)). After WRI, the relative abundance of illite decreased to 71%, accompanied by an increase in both the illite-smectite mixed layer and chlorite proportions (Fig. 2(b)).

3.2 Microscopic mechanical parameters

Indentation measurements unveiled an inherent anisotropy in the mechanical properties of shale at the nanoscale. For pristine shale specimens, the elastic moduli parallel to stratification exhibited a wide range, spanning from 3.7288 to 49.0638 GPa, with an average value of 14.9437 GPa, and the hardness values fluctuated between 0.3768 and 7.8638 GPa, averaging 1.6851 GPa (Fig. 3(a)). In the vertical orientation, the elastic moduli ranged from 2.6406 to 26.9313 GPa, averaging 12.9070 GPa, and the hardness values lied between 0.1489 and 4.9137 GPa, with an average of 1.4244 GPa (Fig. 3(b)).

WRI conspicuously attenuates both the elastic modulus and hardness of the samples. Specifically, in the parallel direction to stratifications, the average elastic modulus diminished to 1.2421 GPa (ranging from 0.7131 to 1.8391 GPa), while the average hardness plunged to 0.2455 GPa (spanning from 0.0924 to 0.4225 GPa) (Fig. 3(c)). In the vertical direction, the elastic modulus experienced an average decline to 5.9036 GPa (ranging from 0.0003 to 12.5014 GPa), and the average hardness was 0.6678 GPa (ranging from 0.0001 to 2.2083 GPa) (Fig. 3(d)).

In the initial state, the microscopic mechanical parameters of shale parallel to stratification were slightly higher than those in the vertical direction, but the difference was very small. The average elastic modulus and hardness of the former were 115.78% and 118.30% of the latter, respectively. WRI not only significantly reduces the microscopic mechanical parameters of shale but also changes the difference in these parameters between parallel and vertical directions to stratification. After WRI, the parameters in the parallel direction were significantly lower than those in the vertical direction. The average elastic modulus and average hardness of the former were 21.04% and 36.76% of the latter, respectively.

3.3 Pores and fractures

The FIB-SEM images of selected samples show varied morphological traits of distinct mineral compositions and

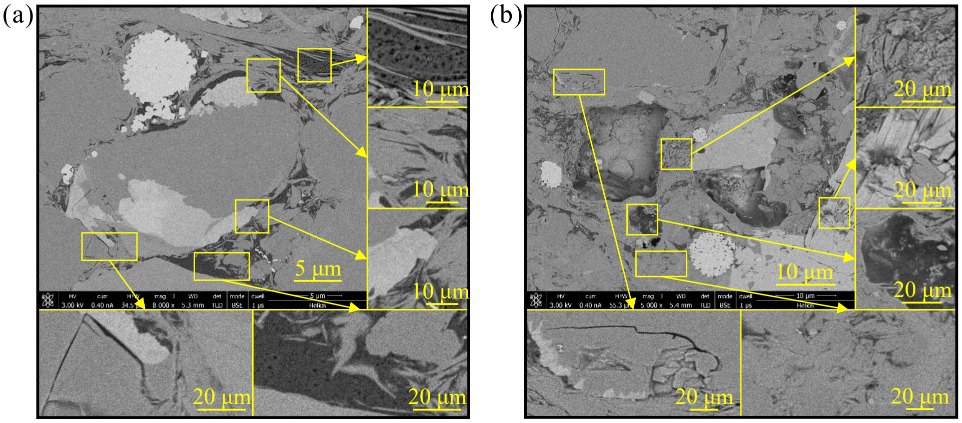

Fig. 4. FIB-SEM images of sample (a) before and (b) after WRI.

micro-pore configurations in the virgin samples (Fig. 4(a)). Organic matter is interspersed among inorganic minerals, displaying minute organic pores arranged in a honeycomb-like pattern with rounded or oval contours. Brittle minerals appear as blocky distributions, accompanied by irregular dissolution pores and slit-like fractures that traverse the matrix in a discontinuous pattern. Clay minerals generally occupy the interstices between organic matter and brittle minerals, exhibiting numerous dissolution pores and interlayer microfractures. Meanwhile, irregular fractures traverse layer boundaries and mineral cementation zones, adopting a strip-like pattern in planar views.

Prior to WRI, the edges of mineral cementation in shale are sharp and distinct, with pores being scarce, isolated and predominantly cylindrical or ink-bottle-shaped, while fractures are short, narrow and infrequent, primarily localized within the cementation of brittle and clay minerals, exhibiting poor overall connectivity (Fig. 4(a)). Following WRI, the edges of mineral cementation blur, particularly in clay-rich regions, leading to an abundance of slit-shaped secondary pores and fractures within both clay and brittle minerals, while fractures evolve into longer, wider and more numerous features, displaying tortuous trajectories and irregular shapes with better connectivity (Fig. 4(b)).

Cross-sectional images obtained via μCT provide clear visualization of the meso-scale fractures inside the shale samples and their evolution over water invasion. In their virgin state, the primary fractures are predominantly confined to the sample stratifications (Figs. 5(a) and 5(e)). Upon the onset of water intrusion, fractures undergo substantial expansion, and notable deterioration and partial detachment are observed at the shale edges (Figs. 5(b) and 5(f)). As the water intrusion extends, further degradation ensues, characterized by the propagation and widening of stratigraphy-oriented fractures, accompanied by the emergence of additional fractures at the stratifications and edges (Figs. 5(c) and 5(g), water intrusion for 102 h). With the advanced stages of water intrusion, a remarkable expansion of interconnected fractures is evident, with their widths increasing from an initial dimension of less than 50 μm to approximately 200 μm (Figs. 5(d) and 5(h), water intrusion for 142 h). This substantial alteration is accompanied by catastrophic damage at the leading edge, marked by the detachment of minerals from the shale matrix (Fig. 5(d)). The original cracks propagate deeply into the matrix, and large-scale cracks also manifest within the matrix regions that were initially devoid of cracks or featured only narrow fractures (Fig. 5(h)). Additionally, near large-scale fractures, a fog-like accumulation of colloids resulting likely from clay hydration is observed, with these recrystallized mineral particles filling some pores and fractures (Fig. 5(g)). In contrast, the strength of secondary reconstruction of water invasion front (Figs. 5(a)-5(d)) is much greater than that of shale matrix (Figs. 5(e)-5(h)).

The 3D model of the samples obtained via μCT enables a quantitative characterization of meso-scale pores and fractures within shale samples. Originally, the pores and fractures exhibited layered and concentrated distribution (Fig. 6(a)). By combining with the μCT images, it can be determined that these cavities are predominantly located within the stratifications. WRI does not alter the distribution characteristics of pores and fractures but renders the pore-fracture network of shale more intricate. A substantial number of secondary pores emerge near the stratifications and the matrix, and large-scale fractures start to expand and extend (Fig. 6(b)). This leads to an increase in rock porosity from 0.08% to 0.28%, as quantified by μCT. WRI significantly influences the pore-fracture network, resulting in a remarkable increase in pore quantity by 1,105.27%, a growth in pore volume by 230.17%, and a rise in surface area by 375.15% (Fig. 6(c)). Notably, the majority of the newly formed structures are composed of pores with diameters less than 300 μm and fractures with diameters exceeding 1,000 μm. Specifically, increases are observed in the proportion of pores with diameters below 300 μm within all pores from 86.70% to 97.72%, their surface area proportion from 28.38% to 63.32%, and their volume proportion from 23.43% to 52.96% (Fig. 6(c)).

As a crucial conduit linking pore structures of diverse scales, pore throats exert a profound impact on the fluid flow characteristics. The pore throat model constructed on the basis of μCT data offers a reliable means for analyzing throat properties. In the pristine state, the throat, akin to pores, exhibits a layered distribution and is concentrated within stratifications (Fig. 7(a)). WRI not only enlarges the pore scale within

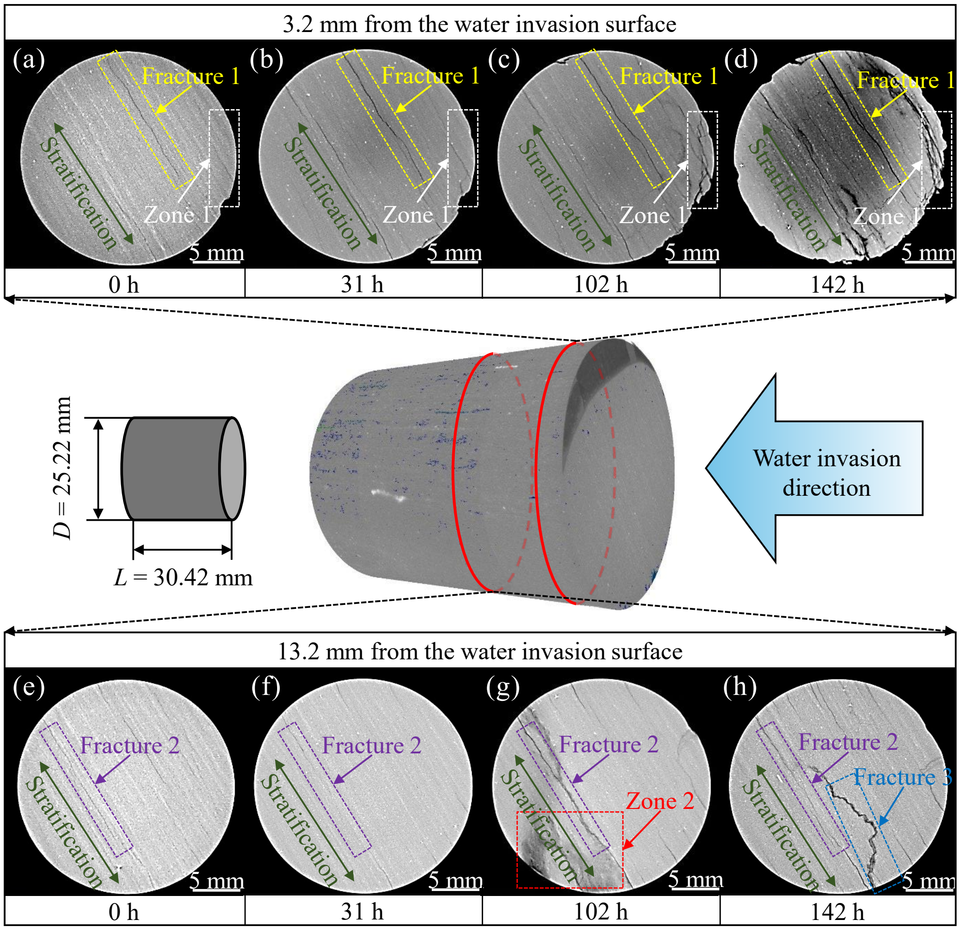

Fig. 5. Representative µCT cross-sectional images.

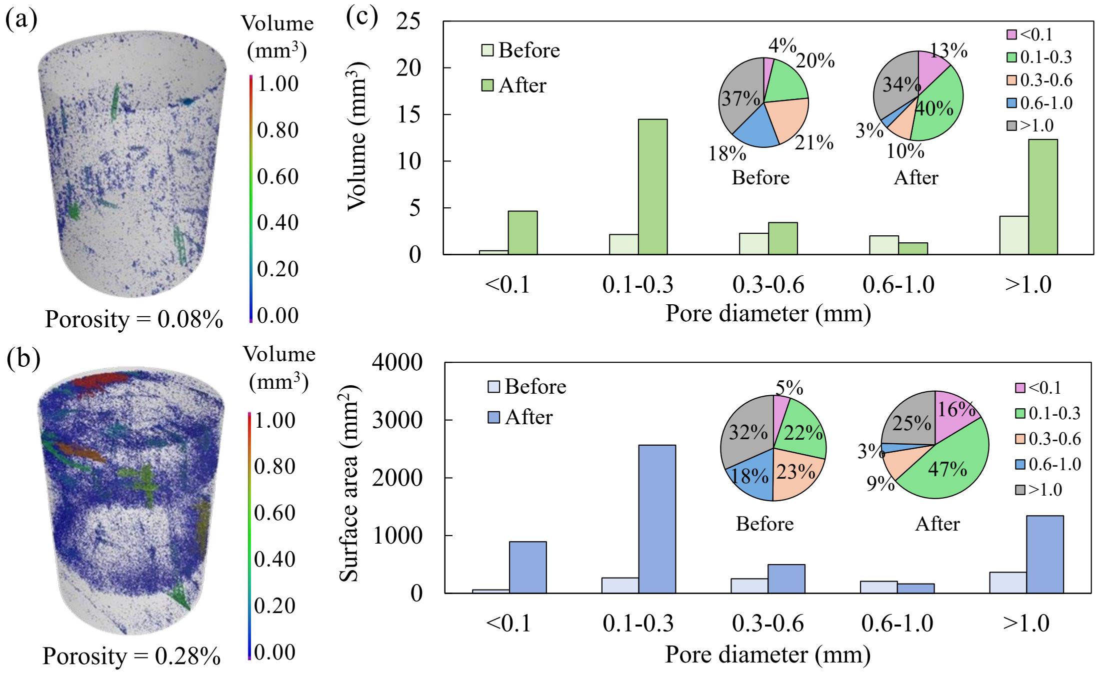

Fig. 6. µCT three-dimensional data volume (a) before and (b) after WRI, (c) the volume and surface area distribution of pores.

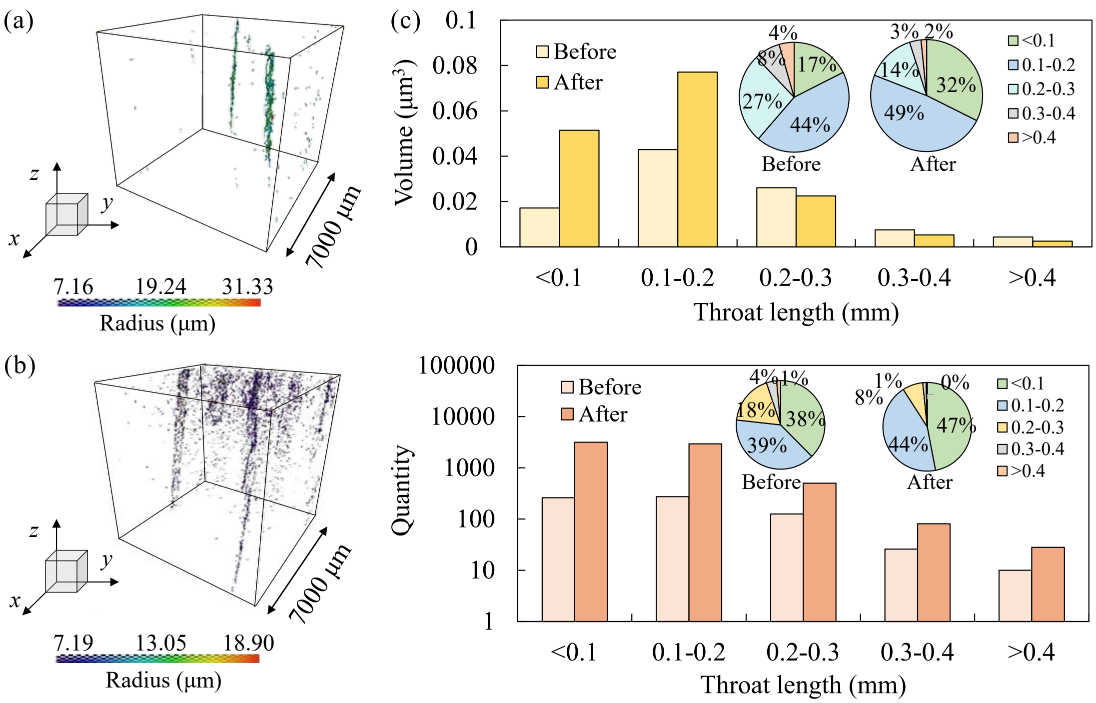

Fig. 7. Pore-throat model (a) before and (b) after WRI, (c) the number and volume distribution of throats.

the stratifications but also augments the connectivity between stratifications (Fig. 7(b)). Moreover, for the pore throat model at the identical position, WRI led to an 861.12% increment in the number of throats and a 61.86% expansion in throat volume (Fig. 7(c)). The majority of the newly added throats are shorter than 200 μm. The quantity of these short throats has surged by 1,038.32%, and their volume has increased by 113.61%. Consequently, the proportion of these short throats within the overall throat population has risen from 76.76% to 90.91%, while their volume proportion has risen from 61.33% to 80.93% (Fig. 7(c)).

4. Discussion

4.1 Alteration of minerals

During shale gas production, multiple fluids like drilling fluid, completion fluid and fracturing fluid are necessarily injected into the reservoir, causing comprehensive alterations to the physical and chemical shale properties, among which the most direct change occurs to shale minerals (Hua et al., 2021; Sui et al., 2018; Yang et al., 2023; Zeng et al., 2020; Zhong et al., 2019). These complex reactions mainly include the hydration of clay minerals, the dissolution of brittle minerals, and the redox of pyrite, which could explain the mineral alteration observed here. In specific, the content of aluminosilicate minerals (predominantly clay minerals) and pyrite declined, while that of quartz and carbonate minerals concomitantly increased.

Clay minerals exhibit the microstructure of plate-like units and this structural feature makes it easier for them to undergo ion hydration, surface hydration, and osmotic hydration upon coming into contact with water (Fig. 8(a)) (Ghasemi and Sharifi, 2021; Deon et al., 2022). The surface of clay mineral particles is charged, which can adsorb ions in the solution and exchange ions, thus changing the chemical composition and properties of minerals (Xue et al., 2018; Zeng et al., 2021). For example, magnesium aluminosilicate can react with hydrogen ions, resulting in the release of magnesium ions and aluminum ions, as well as the formation of new minerals and silicic acid (Wei et al., 2024). Quantitative data show that the overall mass loss of clay is 3.10 g/100 g. Notably, not all clay components exhibited a reduced relative content in that illite indeed witnesses a significant decrease, while the illite-smectite mixed layer and chlorite showed an upward trend. The hydration and mutual transformation significantly reduced the relative content of illite, while the relative content of illite-smectite mixed layer and chlorite increased slightly (Fig. 8(b)). Furthermore, illite underwent a significant mass reduction of 4.82 g/100 g, and the illite-smectite mixed layer and chlorite exhibited increases of 1.28 and 0.67 g/100 g, respectively (Fig. 8(c)). This indicates that illite produces a large amount of aluminum ions, magnesium ions, and silicate ions after hydration. These ions are combined with other ions to recombine and transform into aluminosilicate minerals such as smectite and chlorite.

Certain mineral constituents within shale formations undergo aqueous dissolution, yielding soluble ionic species. A fraction of these dissolved components migrates from the reservoir matrix via flowback fluids, while the remaining portion may undergo secondary precipitation or participate in neomineralization processes under specific physicochemical conditions (e.g., temperature gradients, pressure fluctuations, and pH variations) (Fatah et al., 2022). Plagioclase is a common mineral type in shales and can be decomposed

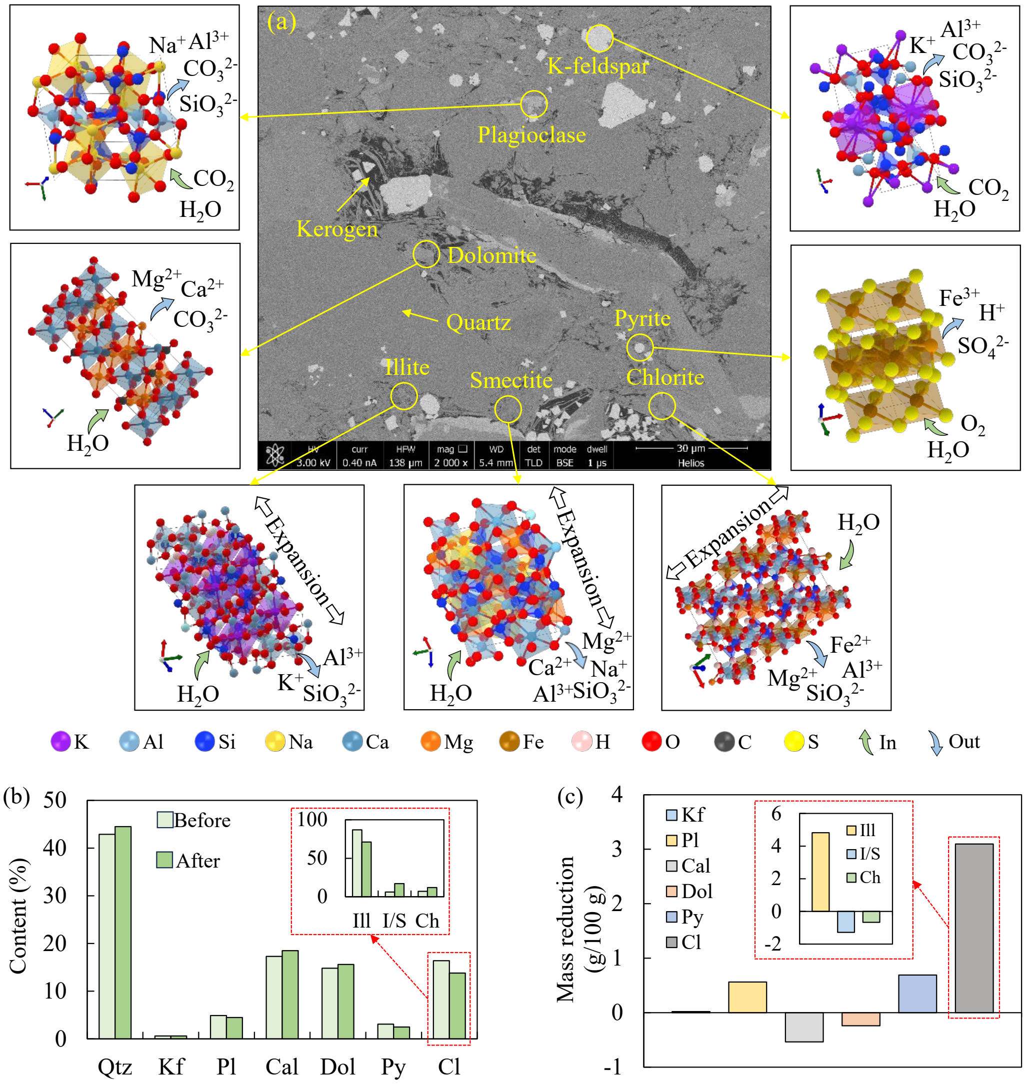

Fig. 8. (a) Water-mineral reaction, (b) relative content of minerals and (c) mineral reduction quality. Qtz: Quartz; Kf: K-Feldspar; Pl: Plagioclase; Cal: Calcite; Dol: Dolomite; Py: Pyrite; Cl: Clay; Ill: Illite; I/S: Illite-smectite mixed layer; Ch: Chlorite.

into silicate minerals and carbonate minerals under the combined action of water and carbon dioxide (Fig. 8(a)) (Liu et al., 2022b). K-feldspar can react with water and carbon dioxide to form potassium bicarbonate and orthosilicic acid, then further react to form kaolinite (Fig. 8(a)) (Liu et al., 2018; Wang et al., 2024). In our experiment, these reactions reduced the mass of plagioclase and potassium feldspar by 0.56 and 0.02 g/100 g, respectively (Fig. 8(c)). Magnesium ions, calcium ions, and carbonate ions in dolomite can be dissolved in water (Fig. 8(a)), while pyrite can react with water and oxygen to form iron ions and sulfuric acid, thus changing the pH value of formation water (Fig. 8(a)) (Emmings et al., 2022). This reaction cannot be ignored. Although the relative content of pyrite in shale is low, its mass is reduced to 0.69 g/100 g under the same conditions. Besides, it may cause acidification of the surrounding environment and further strengthen the WRI (Figs. 8(b) and 8(c)).

The hydration of illite, the dissolution of plagioclase and the redox of pyrite constitute the pivotal processes in the reaction between shale and water. Given that shale harbors a relatively high content of these minerals, it exhibits enhanced WRI intensity.

4.2 Weakening of mechanical properties

Water and shale engage in complex physical and chemical interactions, which subsequently exert an impact on the mechanical attributes and pore architectures of the rock. This phenomenon is mainly caused by the expansion of clay minerals during hydration. The process of clay hydration can be divided into two distinct stages: surface hydration and osmotic hydration. During the surface hydration stage, the lattice expansion of clay particles takes place, accompanied by the adsorption of water molecules, which does not exceed four molecular layers in thickness, resulting in the expansion of crystal layer spacing (Liu et al., 2022a). After the completion of surface hydration, if the cation concentration within the

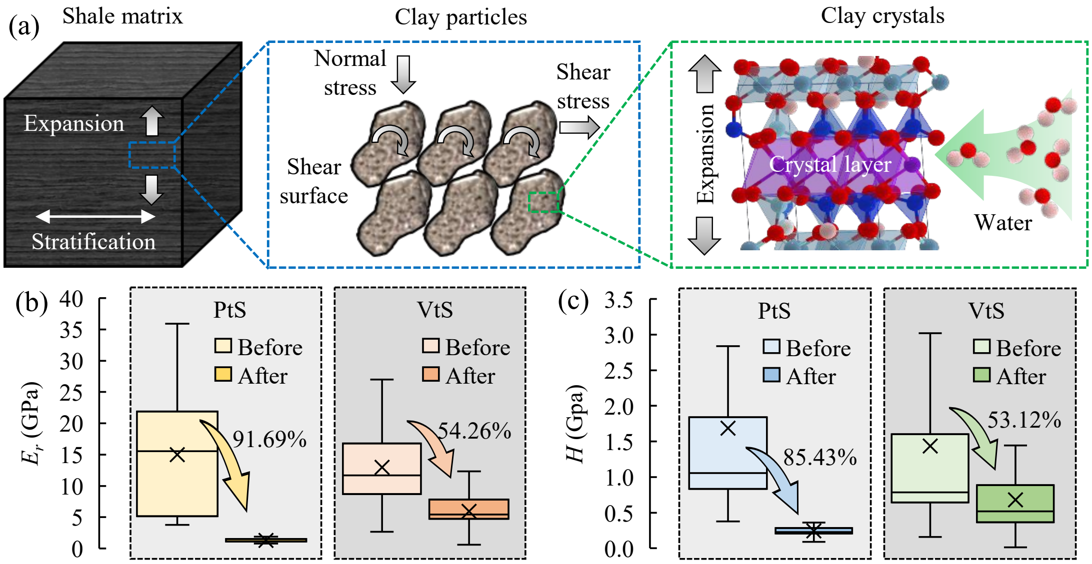

Fig. 9. (a) Weakening mechanism of shale microscopic mechanical parameters, (b) distribution of elastic modulus and (c) distribution of hardness. PtS: Direction parallel to stratifications; VtS: Direction vertical to stratifications.

interlayer spaces exceeds that of the surrounding fluid, water molecules can penetrate into these spaces, leading to an increase in interlayer spacing and the initiation of osmotic hydration. The driving forces behind this stage are osmotic pressure and the repulsive forces within the electric double layer. Osmotic hydration leads to the formation of a diffuse electric double layer, which results in a significantly larger expansion volume compared to lattice expansion alone. This expansion induces stress redistribution within the rock, reduces interparticle cohesion and friction angles, and increases tip stress, collectively leading to a decrease in critical strength (Fig. 9(a)) (Liu et al., 2018). Furthermore, coupled geochemical processes involving the dissolution of feldspar minerals and pyrite redox cycling generate extensive dissolution porosity. This phenomenon structurally compromises the primary lithic fabric, facilitates matrix disaggregation through texture evolution, and ultimately degrades the macro-scale geomechanical integrity of the rock mass to a great extent. Specifically, in the plane parallel to stratifications, the mean elastic modulus of shale samples underwent a dramatic decrement, transitioning from 14.9437 to 1.2421 GPa, and their average hardness experienced a notable reduction, shifting from 1.6851 to 0.2455 GPa (Fig. 9(b)). Correspondingly, in the direction vertical to stratifications, the mean elastic modulus decreased from 12.9070 to 5.9036 GPa, while the average hardness diminished from 1.4244 to 0.6678 GPa (Fig. 9(c)).

Compared to the vertical direction, shale in the parallel direction exhibited greater susceptibility to water. Prior to the WRI, the mechanical parameters measured parallel to stratifications slightly exceeded those measured perpendicular to stratifications, with differences of 13.63% and 15.47% for the average elastic modulus and average hardness, respectively. However, subsequent to WRI, the anisotropy of microscopic mechanical parameters of shale became stronger, with the parameters in the vertical direction substantially surpassing those in the parallel direction. Precisely, for samples measured in the directions parallel and perpendicular to the stratifications, the disparities in average elastic modulus and average hardness reached -375.29% and -172.04%, respectively. This divergence reflects the differential in reaction intensity and effect. The stratifications, harboring more pores and fractures, serve to retain water and facilitate reactions with minerals, thereby augmenting the weakening impact of WRI on the microscopic mechanical properties.

4.3 Expansion of pore-fracture network

The weakening of microscopic mechanical parameters triggers the onset, propagation and interconnection of internal micro-porosity and fractures in shale, while mineral dissolution also contributes to the formation of a substantial quantity of dissolution pores, thereby augmenting porosity and permeability (Figs. 10(a) and 10(b)). The majority of newly emerged pores are of small-scale dimensions, with pore diameters less than 300 μm, with those under 100 μm experiencing the most pronounced increases in number, volume and surface area, surpassing the average values significantly (Fig. 10(c)). These small-scale pores resulted in a 50.95% decrement in the mean throat radius (Fig. 10(d)) and a 3.36% increment in average tortuosity (Fig. 10(e)), indicating the development of a more intricate pore network architecture. Notably, the increase in meso-scale pores (diameters range from 300 to 1,000 μm) was less prominent, and even a decrease was observed in the volume and surface area of pores with diameters ranging from 600 to 1,000 μm, potentially attributed to mineral recrystallization and precipitation processes (Fig. 10(c)). The expansion of clay exerts compressive forces on the adjacent rock matrix, fostering the initiation and progression of microcracks and markedly elevating the count of large-scale fractures (with diameters over 1,000 μm) (Fig. 10(c)). Collectively, these alterations culminate in an augmented porosity of

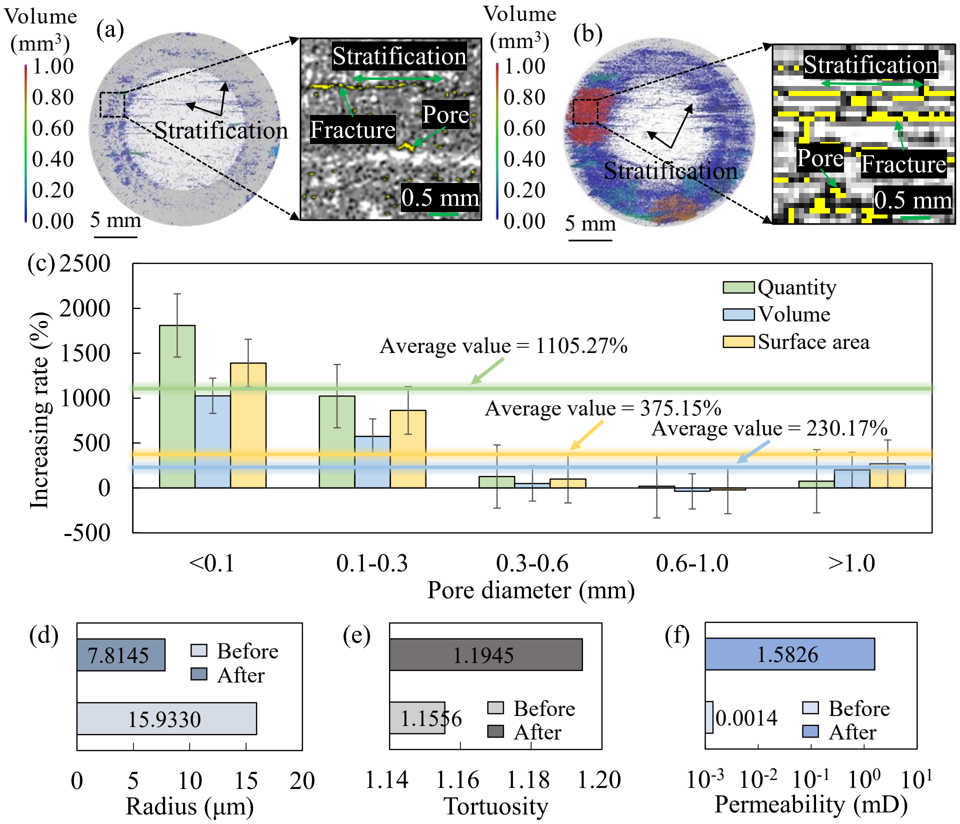

Fig. 10. Pore-fracture network of sample (a) before and (b) after WRI; (c) increasing rates of pore quantity, volume and surface area across various scales; comparison of (d) throat average radius, (e) throat average tortuosity and (f) pulse-decay permeability.

shale and concomitantly enhance gas flow capabilities. This was substantiated by a remarkable escalation in the pulse-decay permeability of the sample, which soared from 0.0014 to 1.5826 mD, representing an 1,129-fold augmentation (Fig. 10(f)).

It is crucial to acknowledge that the above observations stem from controlled laboratory conditions. To mitigate the influence of varying water contents, core samples underwent drying, a process that may not fully emulate the natural developmental mechanisms occurring *in situ*. Despite this constraint, these data impart valuable understanding of the impact of WRI on the secondary reconstruction of shale reservoirs.

4.4 Secondary reconstruction of reservoir

The secondary reconstruction of marine shale by WRI involves the micro-, meso-, and macro-scales (Fig. 11). Stratification is characterized by layered structures where particle arrangement and contact modes at the interfaces are relatively loose, resulting in inferior mechanical properties (Heng et al., 2020). Consequently, these interfaces exhibit heightened susceptibility to deformation and fracturing, giving rise to a pore-fracture network that is either parallel or oblique to the stratification plane. These interfaces also function as preferential zones for fluid accumulation and migration. Fracturing fluids and drilling fluids can infiltrate the shale matrix through these permeable pathways, becoming sequestered within the stratified layers and thereby inducing WRI. The hydration expansion of clay minerals, the dissolution and precipitation dynamics of feldspar minerals, and the redox reactions involving pyrite generate a substantial number of pores and microfractures. The stress concentration arising from clay hydration expansion, coupled with the mechanical weakening due to the dissolution and shedding of feldspar minerals, further facilitates the propagation of fractures. The secondary reconstruction process, driven by WRI, interlinks the initial pores and fractures, augmenting the width and length of existing fractures to form a more intricate pore-fracture network. Consequently, WRI is mainly concentrated in the strata with highly developed primary pores and fractures, which are also the key areas for the secondary reconstruction of shale during hydraulic fracturing and soaking.

It is evident that the minerals within shale engage in intricate interactions with water, carbon dioxide, oxygen, and various other substances, triggering processes such as mineral hydration, dissolution, precipitation, and redox reactions. These complex physical and chemical phenomena exert a significant influence on the mineral composition and mechanical properties of shale, leading to the formation of a substantial number of secondary pores and fractures. This large-scale secondary reconstruction notably improves the seepage capacity of reservoir and facilitates alternative pathways for shale

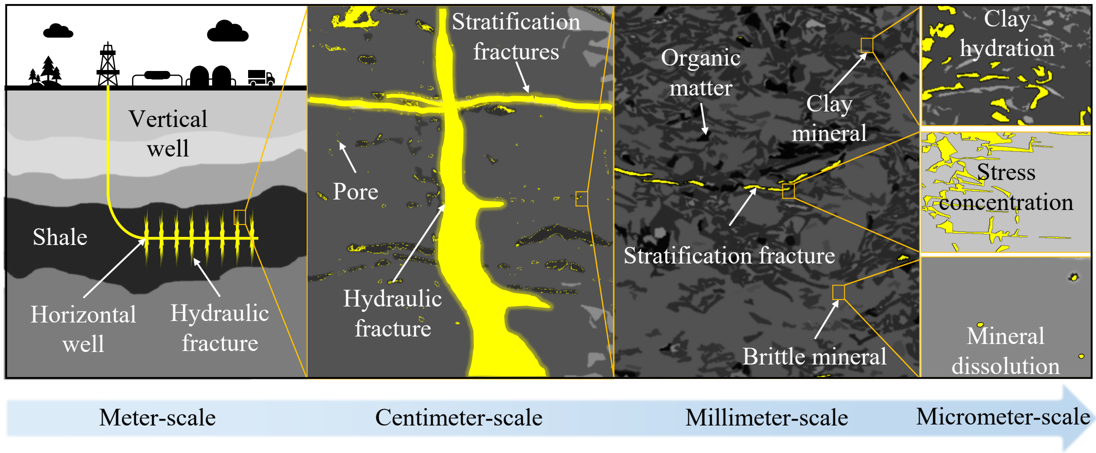

Fig. 11. Multi-scale water-rock interaction of marine shale.

gas migration. Consequently, the secondary reconstruction of marine shale through WRI presents considerable potential for optimization. Various strategies can be effectively utilized to harness this process, including refining hydraulic fracturing schemes, enhancing flowback systems, extending soaking durations, and deploying targeted technologies. These measures collectively aim to augment the pore-fracture network within the reservoir, ultimately enhancing the development potential of shale gas wells and improving their productivity.

5. Conclusions

Hydraulic fracturing and horizontal drilling drive the significant accumulation of working fluids in reservoirs, initiating WRI in marine shales. These interactions induce substantial secondary reconstruction that exert a critical control on shale gas development. To unravel the implications of such WRI-driven reconstruction, we employed XRD, nanoindentation, FIB-SEM, and μCT to systematically characterize the changes in mineral composition, micromechanical properties, and pore-fracture networks. The key observations can be summarized as follows:

1) Water molecules interact with clay minerals via ion hydration, surface hydration and osmotic hydration, facilitating ion release (e.g., K^+, Mg^{2+}, Al^{3+}, $SiO_3{}^{2-}$) and exchange. Feldspars decompose into silicates and carbonates in the presence of water and CO_2, with precipitates forming secondary minerals. Pyrite undergoes redox reactions with water and oxygen, acidifying the surrounding environment and intensifying WRI. After 96 h of immersion, clay mass loss reached 3.10 g/100 g, compared to 0.58 g/100 g for feldspars and 0.69 g/100 g for pyrite. These reactions weaken shale cohesion and initiate pore-fracture network development.
2) Clay hydration-induced crystal expansion redistributes internal stress, reducing interparticle cohesion, friction angles, and critical strength. After 96 h of immersion, samples parallel to stratifications exhibited a 91.69% reduction in average elastic modulus and 85.43% in hardness; the corresponding decreases for vertically oriented samples were 54.26% and 53.12%. Stratification planes are particularly susceptible due to preferential fluid infiltration and mineral reactivity.
3) Mechanical weakening promotes the initiation, propagation and interconnection of pores and microfractures, while the dissolution of intergranular cements drives secondary pore formation and mineral rearrangement. After 142 h of water invasion at 40 MPa, the pore count, volume and surface area increased by 1,212.58%, 230.17% and 375.15%, respectively. Throat abundance rose by 861.12% with a 61.86% volume increase, accompanied by a 50.95% reduction in average throat radius and 3.36% increase in tortuosity. These changes, combined with primary pores and fractures, resulted in the formation of complex networks.
4) Primary pores and fractures, aligned with stratifications, act as preferential pathways for fluid ingress, exacerbating mineral expansion, dissolution and detachment, and amplifying mechanical heterogeneity. Initially, elastic modulus and hardness differed by 13.63% and 15.47% between parallel and perpendicular orientations; post-WRI, these differences shifted to -375.29% and -172.04%, rendering the stratification planes as critical zones for WRI.
5) Newly formed pores and fractures enhance fluid imbibition, further intensifying WRI and pore-fracture network evolution. These dynamics inform optimized hydraulic fracturing designs, including extended soaking and targeted flowback management, in order to boost well productivity.

This study bridges microscopic mechanisms with macroscopic reservoir performance, systematically elucidating WRI-driven secondary reconstruction in marine shales, encompassing mineral hydration and dissolution, micromechanical weakening, and pore-fracture network evolution. The findings provide critical insights for optimizing shale gas development strategies. Future work should integrate real-time monitoring technologies, explore the long-term effects of fracturing fluids under field conditions, and validate the laboratory results *in situ*.

Acknowledgements

This work has been supported by the National Natural Science Foundation of China (Nos. 42202202 and 42472223) and the China National Petroleum Corporation Basic Forward-looking Science and Technology Project (No. 2023ZZ1206). Special thanks are due to the technical staff at the National Energy Shale Gas Research and Development (Experimental) Center, China National Petroleum Corporation Unconventional Oil and Gas Key Laboratory.

Conflict of interest

The authors declare no competing interest.

References

Cai, J., Jiao, X., Wang, H., et al. Multiphase fluid-rock interactions and flow behaviors in shale nanopores: A comprehensive review. Earth-Science Reviews, 2024, 257: 104884.

Chen, X., Eichhubl, P., Olson, J. E. Effect of water on critical and subcritical fracture properties of Woodford shale. Journal of Geophysical Research: Solid Earth, 2017, 122(4): 2736-2750.

Das, D., Mishra, B., Gupta, N. Understanding the influence of petrographic parameters on strength of differently sized shale specimens using XRD and SEM. International Journal of Mining Science and Technology, 2021, 31(5): 953-961.

Dautriat, J., Sarout, J., David, C., et al. Remote monitoring of the mechanical instability induced by fluid substitution and water weakening in the laboratory. Physics of the Earth and Planetary Interiors, 2016, 261: 69-87.

Deon, F., van Ruitenbeek, F., van der Werff, H., et al. Detection of interlayered Illite/Smectite clay minerals with XRD, SEM analyses and reflectance spectroscopy. Sensors, 2022, 22(9): 3602.

Elton, L. R. B., Jackson, D. F. X-ray diffraction and the Bragg law. American Journal of Physics, 1966, 34(11): 1036-1038.

Emmings, J. F., Poulton, S. W., Walsh, J., et al. Pyrite mega-analysis reveals modes of anoxia through geological time. Science Advances, 2022, 8(11): eabj5687.

Fatah, A., Mahmud, H. B., Bennour, Z., et al. Geochemical modelling of CO_2 interactions with shale: Kinetics of mineral dissolution and precipitation on geological time scales. Chemical Geology, 2022, 592: 120742.

Feng, R., Zhang, Y., Rezagholilou, A., et al. Brittleness index: From conventional to hydraulic fracturing energy model. Rock Mechanics and Rock Engineering, 2020, 53(2): 739-753.

Garum, M., Glover, P. W. J., Lorinczi, P., et al. Micro- and nano-scale pore structure in gas shale using Xμ-CT and FIB-SEM techniques. Energy & Fuels, 2020, 34(10): 12340-12353.

Ghasemi, M., Sharifi, M. Effects of layer-charge distribution on swelling behavior of mixed-layer illite-montmorillonite clays: A molecular dynamics simulation study. Journal of Molecular Liquids, 2021, 335: 116188.

Heng, S., Li, X., Liu, X., et al. Experimental study on the mechanical properties of bedding planes in shale. Journal of Natural Gas Science and Engineering, 2020, 76: 103161.

Hua, G., Wu, S., Jing, Z., et al. Rock physical and chemical alterations during the in-situ interaction between fracturing fluid and Silurian organic-rich shales in China. Journal of Natural Gas Science and Engineering, 2021, 94: 104075.

Jing, Z., Balucan, R. D., Underschultz, J. R., et al. Oxidant stimulation for enhancing coal seam permeability: swelling and solubilisation behaviour of unconfined coal particles in oxidants. Fuel, 2018a, 221: 320-328.

Jing, Z., Mahoney, S. A., Rodrigues, S., et al. A preliminary study of oxidant stimulation for enhancing coal seam permeability: Effects of sodium hypochlorite oxidation on subbituminous and bituminous Australian coals. International Journal of Coal Geology, 2018b, 200: 36-44.

Jin, Z., Nie, H., Liu, Q., et al. Source and seal coupling mechanism for shale gas enrichment in upper Ordovician Wufeng Formation - Lower Silurian Longmaxi Formation in Sichuan Basin and its periphery. Marine and Petroleum Geology, 2018, 97: 78-93.

Kang, Y., She, J., Zhang, H., et al. Strengthening shale wellbore with silica nanoparticles drilling fluid. Petroleum, 2016, 2(2): 189-195.

Kelly, S., El-Sobky, H., Torres-Verdín, C., et al. Assessing the utility of FIB-SEM images for shale digital rock physics. Advances in Water Resources, 2016, 95: 302-316.

Lin, H., Sun, X., Yuan, Y., et al. Experimental investigation on the dynamic volume changes of varied-size pores during shale hydration. Journal of Natural Gas Science and Engineering, 2022, 101: 104506.

Li, N., Zhou, T., Zhao, M., et al. Thermal-shock-induced surface softening and conductivity evolution of hydraulic fracture in enhanced geothermal system. Geothermics, 2022, 102: 102405.

Liu, B., Fu, X., Li, Z. Impacts of CO_2-brine-rock interaction on sealing efficiency of sand caprock: A case study of Shihezi formation in Ordos basin. Advances in Geo-Energy Research, 2018, 2(4): 380-392.

Liu, G., Liu, K., Zhai, G., et al. Crystallinity and formation of silica in Palaeozoic shales: A new quantification calculation method based on X-Ray diffraction. Marine and Petroleum Geology, 2023, 150: 106124.

Liu, K., Ostadhassan, M., Bubach, B. Applications of nano-indentation methods to estimate nanoscale mechanical properties of shale reservoir rocks. Journal of Natural Gas Science and Engineering, 2016a, 35: 1310-1319.

Liu, K., Ostadhassan, M., Bubach, B., et al. Nano-dynamic mechanical analysis (nano-DMA) of creep behavior of shales: Bakken case study. Journal of Materials Science, 2018, 53(6): 4417-4432.

Liu, X., Zeng, W., Liang, L., et al. Experimental study on hydration damage mechanism of shale from the Longmaxi

Formation in southern Sichuan Basin, China. Petroleum, 2016b, 2(1): 54-60.

Liu, Y., Liu, A., Liu, S., et al. Nano-scale mechanical properties of constituent minerals in shales investigated by combined nanoindentation statistical analyses and SEM-EDS-XRD techniques. International Journal of Rock Mechanics and Mining Sciences, 2022a, 159: 105187.

Liu, Y., Yang, C., Wang, J., et al. New insights into hydration-induced creep behavior of shale: A comparison study of brittle black shale and clayey oil shale at micro-scale. Marine and Petroleum Geology, 2022b, 138: 105554.

Lu, Y., Li, Y., Wu, Y., et al. Characterization of shale softening by large volume-based nanoindentation. Rock Mechanics and Rock Engineering, 2020, 53(3): 1393-1409.

Lyu, Q., Long, X., Ranjith, P. G., et al. Experimental investigation on the mechanical properties of a low-clay shale with different adsorption times in sub-/super-critical CO_2. Energy, 2018, 147: 1288-1298.

Ma, T., Yang, C., Chen, P., et al. On the damage constitutive model for hydrated shale using CT scanning technology. Journal of Natural Gas Science and Engineering, 2016, 28: 204-214.

Molčanov, K., Stilinovič, V. Chemical crystallography before X-ray diffraction. Angewandte Chemie International Edition, 2014, 53(3): 638-652.

Richter, A., Ries, R., Smith, R., et al. Nanoindentation of diamond, graphite and fullerene films. Diamond and Related Materials, 2000, 9(2): 170-184.

Roshan, H., Ehsani, S., Marjo, C. E., et al. Mechanisms of water adsorption into partially saturated fractured shales: An experimental study. Fuel, 2015, 159: 628-637.

Røyne, A., Dalby, K.N., Hassenkam, T. Repulsive hydration forces between calcite surfaces and their effect on the brittle strength of calcite-bearing rocks. Geophysical Research Letters, 2015, 42(12): 4786-4794.

Song, J., Xiang, D., Hu, D., et al. Creep characteristics of a fracturing fluid-softened shale investigated by microindentation. International Journal of Rock Mechanics and Mining Sciences, 2022, 152: 105067.

Sui, W., Tian, Y., Yao, C. Investigation of microscopic pore structure variations of shale due to hydration effects through SEM fixed-point observation experiments. Petroleum Exploration and Development, 2018, 45(5): 955-962.

Tang, J., Lan, T., Lai, Y., et al. Softening mechanism and characteristics of mudstone after absorbing moisture. Applied Clay Science, 2024, 254: 107398.

Thibault, P., Elser, V. X-Ray Diffraction Microscopy. Annual Review of Condensed Matter Physics, 2010, 1: 237-255.

Velcin, H., Dautriat, J., Sarout, J., et al. Experimental reactivation of shear-fractured berea and boise sandstones by brine or liquid CO_2 injection at depth. Journal of Geophysical Research: Solid Earth, 2020, 125(2): e2019JB018281.

Wang, Y., Liu, X., Liang, L., et al. Experimental study on the damage of organic-rich shale during water-shale interaction. Journal of Natural Gas Science and Engineering, 2020, 74: 103103.

Wang, Y., Zhang, P., Wang, Z., et al. The role of water in the change of the fracture toughness during the $ScCO_2$ interactions with shale samples. Journal of CO_2 Utilization, 2024, 85: 102883.

Wei, Z., Wang, M., Shan, W., et al. Synergistic effects of potassium alginate and silicates co-inhibition performance in shale hydration. Journal of Molecular Liquids, 2024, 393: 123538.

Xu, S., Zhou, S., Zhou, J., et al. Multiscale pore structure evolution of Longmaxi shale induced by acid treatment. SPE Journal, 2023, 28(2): 831-844.

Xue, H., Zhou, S., Jiang, Y., et al. Effects of hydration on the microstructure and physical properties of shale. Petroleum Exploration and Development, 2018, 45(6): 1146-1153.

Yang, C., Xiong, Y., Zhang, J. A comprehensive re-understanding of the OM-hosted nanopores in the marine Wufeng–Longmaxi shale formation in South China by organic petrology, gas adsorption, and X-ray diffraction studies. International Journal of Coal Geology, 2020, 218: 103362.

Yang, J., Sun, J., Wang, R., et al. Treatment of drilling fluid waste during oil and gas drilling: A review. Environmental Science and Pollution Research, 2023, 30(8): 19662-19682.

Zeng, F., Zhang, Q., Guo, J., et al. Mechanisms of shale hydration and water block removal. Petroleum Exploration and Development, 2021, 48(3): 752-761.

Zeng, L., Chen, Y., Lu, Y., et al. Role of brine composition on rock surface energy and its implications for subcritical crack growth in calcite. Journal of Molecular Liquids, 2020, 303: 112638.

Zhong, Y., Kuru, E., Zhang, H., et al. Effect of fracturing fluid/shale rock interaction on the rock physical and mechanical properties, the proppant embedment depth and the fracture conductivity. Rock Mechanics and Rock Engineering, 2019, 52(4): 1011-1022.

Zhou, S., Yan, G., Xue, H., et al. 2D and 3D nanopore characterization of gas shale in Longmaxi formation based on FIB-SEM. Marine and Petroleum Geology, 2016a, 73: 174-180.

Zhou, T., Zhang, S., Yang, L., et al. Experimental investigation on fracture surface strength softening induced by fracturing fluid imbibition and its impacts on flow conductivity in shale reservoirs. Journal of Natural Gas Science and Engineering, 2016b, 36: 893-905.

Zou, C., Zhao, Z., Pan, S., et al. Unveiling the oldest industrial shale gas reservoir: Insights for the enrichment pattern and exploration direction of lower cambrian shale gas in the Sichuan Basin. Engineering, 2024, 42: 278-294.